Materials Today Bio 32 (2025) 101741

Contents lists available at ScienceDirect

Materials Today Bio

journal homepage: www.journals.elsevier.com/materials-today-bio

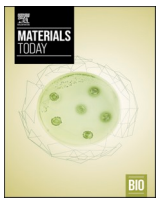

A vascularized tumors-on-a-chip model for studying tumor-angiogenesis interplay, heterogeneity and drug responses

Suyeon Shin [a,1], Yurim Choi [a,1], WonJun Jang [b], Batjargal Ulziituya [b], Giheon Ha [a], Raehui Kang [d], Soojin Park [b], Minseok Kim [b], Yu Shrike Zhang [c], Han-Jun Kim [b,*], Junmin Lee [a,**]

[a] Department of Materials Science and Engineering, Pohang University of Science and Technology (POSTECH), Pohang, 790-784, Republic of Korea
[b] College of Pharmacy, Korea University, Sejong, 30019, Republic of Korea
[c] Division of Engineering in Medicine, Department of Medicine, Brigham and Women's Hospital, Harvard Medical School, Cambridge, 02139, MA, USA
[d] Division of Interdisciplinary Bioscience & Bioengineering, Pohang University of Science and Technology (POSTECH), Pohang, 790-784, Republic of Korea

ARTICLE INFO

Keywords:
Tumor-vessel interaction
Vascularized tumor model
Tumor microenvironment (TME)
Tumors-on-a-chip

ABSTRACT

Current tumor models struggle to replicate the complexity of the tumor microenvironment, particularly endothelial sprouting and vascular-tumor interactions. To address these limitations, we developed a vascularized tumors-on-a-chip model by fusing tumor spheroids with HUVEC spheroids to simulate angiogenesis. The model incorporates hypoxia-driven cytokine secretion and dynamic endothelial penetration, enabling accurate recapitulation of angiogenic processes. Spheroids were optimized for size and viability, and four cancer types were studied, with GBM and A549 exhibiting the highest angiogenic potential, as confirmed by Z-stack imaging and qRT-PCR. Encapsulation in GelMA and integration into PDMS-based microfluidic chips provided a dynamic flow environment, mimicking *in vivo* drug delivery while enabling high-throughput drug screening. This chip-based system allows simultaneous testing of multiple drugs or tumors under physiologically relevant conditions, enhancing its translational potential. The platform was validated using doxorubicin and bevacizumab, revealing reduced VEGF secretion and dynamic cytokine responses, replicating vascular barriers. Further validation in murine models demonstrated its capacity to promote angiogenesis and mimic tumor-vessel interactions. This advanced tumors-on-a-chip model addresses critical shortcomings of conventional 2D and 3D systems and offers a transformative tool for preclinical drug evaluation and the development of precision oncology strategies, bridging the gap between *in vitro* testing and *in vivo* relevance.

1. Introduction

Cancer remains a significant public health concern and is the second leading cause of death in the United States, despite ongoing research and a steady decline in mortality rates since 1991 [1]. Cancer is not solely characterized by abnormally proliferating malignant cells; the tumor microenvironment (TME) is a complex structure comprising various cell types and extracellular matrix (ECM) components. The TME includes fibroblasts, immune cells, vascular endothelial cells, stromal cells, and cancer cells [2]. While non-malignant, these cells contribute to cancer progression by releasing cytokines and growth factors in response to interactions with cancer cells. Vascular endothelial cells are particularly critical not only in forming the tumor's vasculature but also in facilitating tumor growth and metastasis by regulating oxygen and nutrient supply and modulating immune responses [3]. As cancer cells proliferate and the tumor enlarges, the supply of oxygen and nutrients becomes insufficient. As the TME becomes increasingly hypoxic, ischemic and acidic and experiences elevated interstitial pressure, cancer cells release growth factors and cytokines, promoting angiogenesis [4]. This process involves tumor-driven activation, migration, and sprouting of endothelial cells toward and into the tumor spheroid, ultimately leading to the formation of capillary-like structures.

Given the critical role of angiogenesis in cancer progression, numerous studies have focused on mimicking angiogenesis *in vitro* to

* Corresponding author.
** Corresponding author.
E-mail addresses: hanjun@korea.ac.kr (H.-J. Kim), junmin@postech.ac.kr (J. Lee).
[1] These authors contributed equally to this work.

https://doi.org/10.1016/j.mtbio.2025.101741
Received 18 February 2025; Received in revised form 4 April 2025; Accepted 6 April 2025
Available online 8 April 2025

better understand tumor behavior and develop potential therapies. To mimic angiogenesis, three-dimensional (3D) spheroid cultures have emerged as alternatives to traditional two-dimensional (2D) cultures for studying angiogenesis. These 3D cultures effectively replicate the oxygen and nutrient gradients found in tumors and enable enhanced cell-cell interactions, making them more representative of the in-vivo environment [5]. Moreover, co-culturing multiple cell types within spheroids offers a more accurate reflection of tumor complexity, capturing key biological processes such as cellular responses, drug resistance mechanisms, and angiogenesis [6]. For these reasons, multicellular tumor spheroid (MCTS) models, incorporating cancer cells, fibroblasts, and human umbilical vein endothelial cells (HUVECs), have been extensively studied. Encapsulation of MCTs in fibrin gel has shown that endothelial cells exhibit sprouting behavior, form luminal structures, and support tumor growth [7]. Furthermore, vascularized MCTS models with HUVEC-encapsulated gels demonstrated that endothelial cells create tubular structures connecting to the MCTS, allowing fluid flow through the vessel [8]. However, these models are limited in their ability to fully replicate angiogenesis, particularly in simulating the detailed signaling pathways where endothelial cells receive guidance signals and migrate as tip cells toward the tumor [9]. This limitation restricts their ability to capture critical aspects of tumor vascularization and its impact on cancer progression.

Spheroid models that simulate real tumor environments are increasingly being used to test new drugs *in vitro*. The development of target therapies, such as anti-angiogenic drugs, has expanded beyond traditional chemotherapy, aiming to block tumor angiogenesis by targeting the tumor microenvironment [10] as well as vascular endothelial growth factor-A (VEGF-A; VEGF) and other pro-angiogenic pathways 4a, 11. These advancements have further informed the use of vascularized tumor spheroid models to assess drug efficacy. Such models are essential since the TME, particularly endothelial cells, presents a significant barrier to effective drug delivery in solid tumors [12]. In the vascular system, solutes—including most drugs except small lipophilic molecules—must navigate narrow intercellular clefts in the endothelial layer, hindering effective delivery [12b]. Vascularized tumor models have been shown to replicate these challenges, with studies demonstrating that drug penetration occurs more slowly in vascularized MCTs, highlighting their potential as an effective platforms for *in vitro* drug efficacy testing [13]. Furthermore, recent studies have incorporated vascularized tumors into microfluidic chips to develop high-throughput drug screening platforms [14]. However, many of these platforms focus on chip fabrication, which could be challenging to manufacture and may suffer from low throughput. Additionally, comparative studies of drug screening across cancers of various organs remain limited.

Here, we present a tumor-HUVEC fusion system, designed as a vascularized tumor model to observe the angiogenesis process. This system is established by fusing independently formed spheroids of tumor cells and HUVECs, which leads to the formation of endothelial sprouts. We compared the angiogenic potential of tumors derived from cancer cells of different organs, identifying those with the highest angiogenic activity by measuring the extent of HUVEC sprouting toward tumors. The vascularized tumor with the highest angiogenic potential was encapsulated in a gel and applied to a fluidic chip to create a more realistic environment, demonstrating its applicability for drug efficacy testing. Through this fluidic chip application, we enabled comparative analysis of drug responses in various organ cancers and intra-organ cancer cells within a single device. Additionally, the hydrogels encapsulating tumor-HUVEC fused spheroids was implanted into mouse subcutaneous tissue, where it effectively promoted angiogenesis *in vivo*. By better illustrating angiogenesis processes in tumor environments and more accurately mimicking the interaction between tumors and HUVECs, this model would be useful as a platform for testing new anti-angiogenic drugs.

2. Results and discussion

2.1. Optimization of spheroids

In this study, we aim to mimic the process where cancer cell clusters form a tumor that secretes angiogenic factors, resulting in endothelial cell sprouting (Fig. 1). To replicate the gradient and hypoxic environment characteristic of tumors and to simulate blood vessels with strong cell-cell interactions (as observed in HUVECs), cells were cultured in 3D. Among the available 3D culture methods, spheroid culture was selected due to its simplicity and reproducibility. Although various spheroid fabrication methods exist [15], we used the widely available commercial AggreWell system for spheroid production [16]. The first step in our study was optimizing spheroid size. Establishing standardized spheroid size and viability was not only necessary for minimizing hypoxia-induced variability, but also essential for ensuring reproducible endothelial fusion and angiogenic behavior across tumor types.

To identify four cancer cell types and spheroid size suitable with fusion model, we screened various cancer cell types derived from different organs. The morphology of these spheroids was evaluated by measuring diameter and circularity. A spheroid diameter limit of 400 μm was established to avoid the formation of a hypoxic core [17]. Based on this criterion, the condition of 5000 cells per spheroid was excluded, and ultimately a condition of 3000 cells per spheroid was selected (Fig. S1). Additionally, four cancer cell types with high circularity and similar diameters were chosen (Fig. 2A and B): A549 (lung carcinoma), 5637 (bladder carcinoma), Capan-2 (pancreatic adenocarcinoma), and SNU-1105 (GBM; brain glioblastoma) (Fig. 2C).

Given the lower oxygen and nutrient levels in spheroid cultures compared to 2D cultures, a cell viability assessment was conducted. By day 4, all tumor spheroids exhibited over 80 % viability (Fig. 2D). Long-term cell viability was further evaluated to assess the suitability for co-culture experiments, with A549 spheroids maintaining over 80 % viability until day 16 (Fig. 2E and F). Based on the stabilization of cell morphology from day 5 and sustained high viability before day 16, 4-day-old tumor spheroids were selected for tumor-HUVEC fusion system.

For HUVEC spheroids, size compatibility with tumor spheroids was ensured. Two conditions (1500 cells/spheroid and 3000 cells/spheroid) were tested at tumor-to-HUVEC ratios of 1:1 and 2:1 (Fig. 2G). After 24 h of culture, both conditions showed circularity greater than 0.8 (Fig. 2H). However, 1500 cells per spheroid were selected due to their comparable diameter to the tumor spheroids (Fig. 2I). As a result, 4-day-old tumor spheroids (3000 cells/spheroid) and 1-day-old HUVEC spheroids (1500 cells/spheroid) were chosen for tumor-HUVEC fusion system.

2.2. Angiogenic ability of tumors in 2D culture

To gain preliminary insights into tumor effects on HUVECs before exploring sprout-driven angiogenesis in 3D, we first analyzed interactions in 2D. HUVECs grown in tumor spheroid-conditioned medium (CM) were used to evaluate the influence of tumor cytokines on angiogenesis through tube formation, migration, and proliferation assays [18].

The HUVEC vascularization potential was first assessed using a tube formation assay, which effectively recapitulates key steps of angiogenesis [19]. Using GBM- CM as a preliminary model, 24 h of incubation was established as the standard imaging point due to notable differences from the control (Fig. S2). Under tumor CM conditions, HUVECs migrated and formed capillary-like network structure (Fig. 3B). Quantitative analysis using metrics such as total tube length, junction numbers, mesh numbers, and mesh area revealed significant differences between groups. The 5637 group demonstrated values close to the control, while the other groups (Capan-2, A549, and GBM) exhibited superior angiogenic potential, with GBM showing the most robust capillary structure formation (Fig. 3C–F).

Subsequently, HUVEC migration was assessed using a wound healing

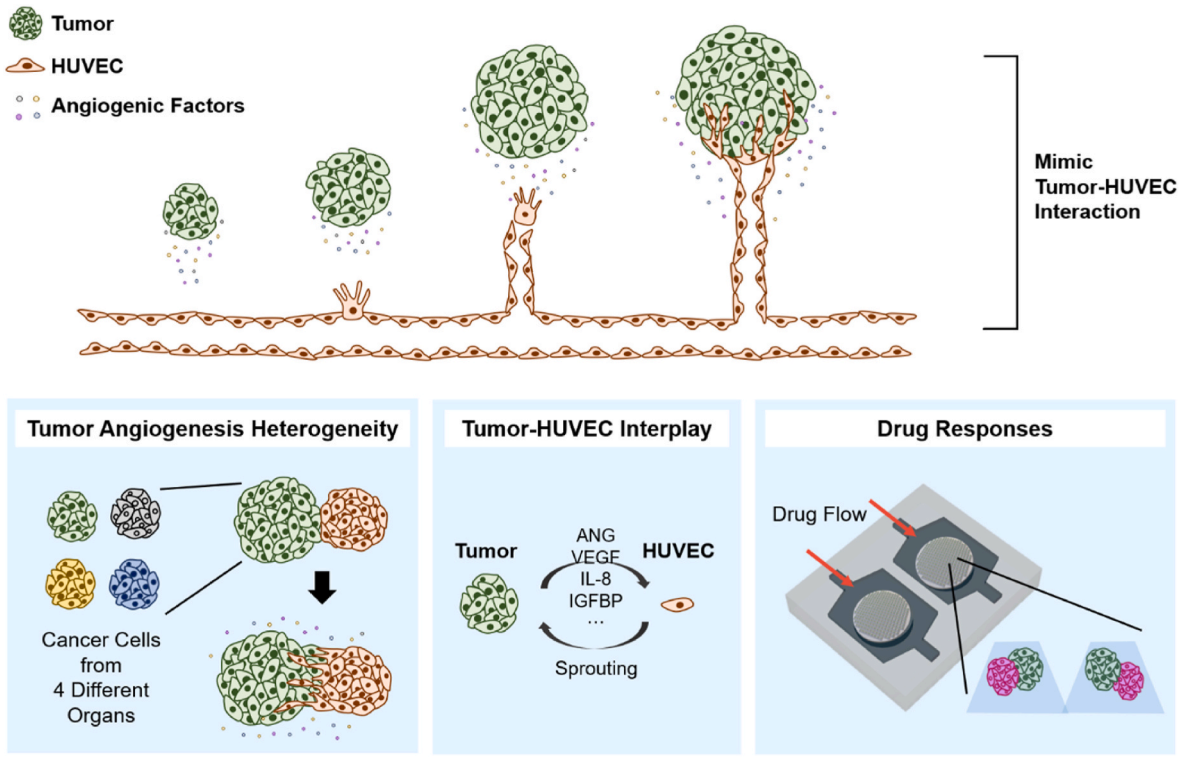

Fig. 1. Illustration of tumor angiogenesis and tumor-HUVEC fusion model.

assay. Immediately after the wound was induced, all groups presented similar widths of cell-free areas, but over 48 h, cells migrated to fill this area (Fig. 3G). Compared to the control, cell movement into the cell-free region was increased in all tumor CM groups except for 5637 CM, where differences in coverage became significantly larger over time (Fig. 3H). From 36 h onward, capan-2, A549, and GBM demonstrated noticeably greater area coverage, and by 48 h, they had recovered over 70 % (0.74 $\pm$ 0.126) for capan-2 and 0.78 $\pm$ 0.099 for GBM). A549, in particular, achieved over 80 % (0.88 $\pm$ 0.029), indicating that tumor CM effectively enhances HUVEC migration.

Lastly, the WST-8 assay was used to evaluate HUVEC proliferation. An increase in absorbance at 450 nm indicates a higher cell count, reflecting active cell proliferation. Results showed that absorbance increased over the 48-h period across all groups, indicating cell growth. HUVEC proliferation in 5637 CM was similar to that of the control (Fig. 3I). In contrast, proliferation was significantly elevated in the capan-2, A549, and GBM CM groups from 24 h, with significant differences relative to the control over time (Fig. 3J–L). At 48 h, absorbance values for capan-2, A549, and GBM were 0.357 $\pm$ 0.012, 0.402 $\pm$ 0.014, and 0.404 $\pm$ 0.037, respectively, significantly exceeding the control's 0.295 $\pm$ 0.017 ($p < 0.01$), indicating that tumor CM enhances HUVEC proliferation.

Evaluations of angiogenesis-related activities—tube formation, migration, and proliferation—showed similar trends across the assays. In each assay, capan-2, A549, and GBM CM showed significantly higher angiogenic activity compared to the control, while 5637 CM showed similar results to the control. This observation implies that tumor spheroid-derived secretions could independently promote angiogenesis in HUVECs. Specifically, factors within the secretions may enhance HUVEC migration and proliferation, as evidenced by this study.

2.3. Formation of tumor-HUVEC fusion system

Building upon 2D angiogenesis studies, we aimed to replicate angiogenesis in a 3D environment by designing a spheroid fusion system. To induce fusion, tumor spheroids with established oxygen and nutrient gradients were co-cultured with HUVEC spheroids, which exhibited pre-established cell-cell interactions. The transfer process was optimized to achieve a consistent and reliable fusion system. Based on the spheroid optimization results (Fig. 2), tumor spheroids were cultured for 4 days and HUVEC spheroids for 1 day to ensure uniform conditions (Fig. 4A and G). Tumor cells were labeled in green, while HUVECs were labeled in red for visualization.

Initially, tumor spheroids were transferred to HUVEC spheroids by pipetting. Large-scale imaging results of the transfer of 5637 tumor spheroids into wells containing HUVEC spheroids. It showed that red HUVEC spheroids maintained their structure within the microwell, whereas green tumor spheroids tended to lost their shape and dispersed (Fig. 4B). This phenomenon was observed across several cancer cell types. Quantitative analysis revealed that more than 60 % of wells containing 5637 or Capan-2 cells consisted primarily of single cells surrounding the HUVEC spheroid, while GBM spheroids transferred intact in approximately 30 % of wells (Fig. 4C). Images revealed that 5637, Capan-2, and A549 spheroids displayed a mix of single cells around the HUVEC spheroid (Fig. 4B and E). In contrast, GBM spheroids largely remained their structural integrity, with minimal single-cell dispersion around the HUVEC spheroids (Fig. 4F). These differences in aggregation stability were likely due to varying degrees of cell-cell interactions among the different cancer cell types [20]. The variations in transfer efficiency across cancer cell type highlighted the need for a revised transfer protocol to established a uniform fusion system.

Reversing the transfer direction, HUVEC spheroids were pipetted into tumor spheroids while maintaining the same timeline. This approach produced more consistent results. For instance, when HUVEC spheroids were transferred into 5637 spheroids, imaging revealed fewer single cells scattered in the microwell, and the spheroid structure remained more intact (Fig. 4H). The spherical shape of HUVEC spheroids was maintained, and their diameters were uniform across all tumor spheroid wells. Quantitative analysis corroborated these observations, showing that around 40 % of microwells contained one or more HUVEC spheroids across all cancer types (5637, capan-2, A549, GBM) (Fig. 4I). Based on these results, the HUVEC-to-tumor spheroid transfer method

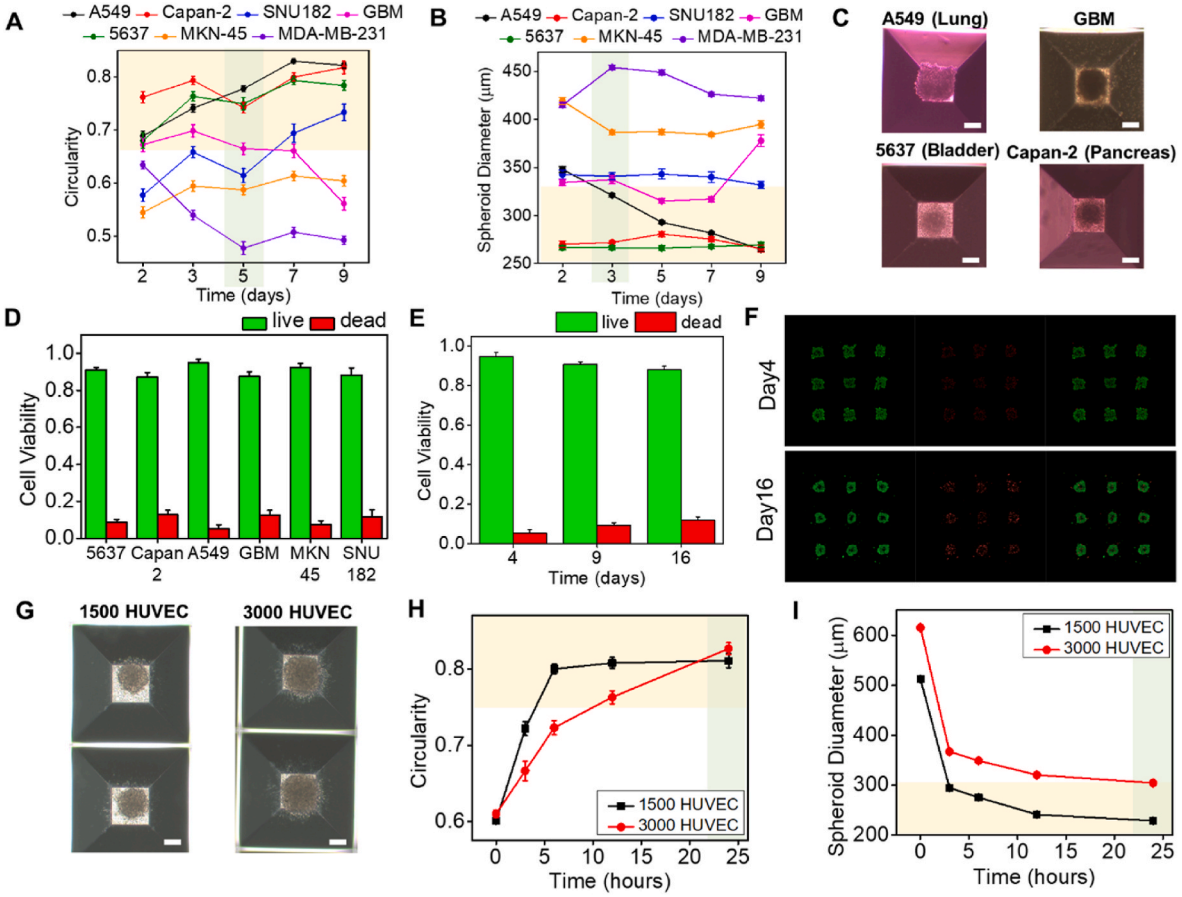

Fig. 2. Optimization of spheroid conditions for experimental setting. (A) Spheroid circularity of 3000 cells/spheroid tumor spheroids. (B) Spheroid diameter of 3000 cells/spheroid tumor spheroids. (C) Representative optical images for tumor spheroids. (D) Cell viability of A549 spheroid at day4, 9 and 16. (E) Cell viability of tumor spheroids at day4. (F) Representative confocal 3D images of live(green)/dead(red) cells in A549 spheroids at day4 and 16. (G) Representative optical images for HUVEC spheroids. (H) Spheroid circularity of 1500, 3000 cells/spheroid HUVEC spheroids. (I) Spheroid diameter of 1500, 3000 cells/spheroid HUVEC spheroids. Scale bars are all 100 μm. (For interpretation of the references to color in this figure legend, the reader is referred to the Web version of this article.)

was selected as the optimal approach to ensure consistent morphology across different cancer types.

2.4. Angiogenic penetration in 3D system

Using the HUVEC-to-tumor transfer method, a tumor-HUVEC fusion system was established to observe tumor-endothelial interactions over a seven-day co-culture period. Tumor spheroids were labeled in green, and HUVECs in red, enabling cell tracking and imaging every two-day intervals to monitor morphological changes during fusion. Morphological alterations due to spheroid interactions became apparent over time (Fig. 5A). Key observable changes were chosen as indicators for analysis, focusing on the overall area of the fused spheroids and the extent of HUVEC penetration into the tumor spheroid.

The first metric analyzed was the area of the fused spheroids, defined as the combined area of tumor and HUVEC spheroids. Over time, the fused spheroid area showed a decreasing trend (Fig. 5B). The 5637 and Capan-2 spheroids reduced by approximately 10 % by day 3 and stabilized, while A549 and GBM continued decreasing until day 7. In results, A549 and GBM fused spheroids exhibited significant size reductions in day 7 compared to other tumor types (Fig. 5C). Subsequently, HUVEC penetration into tumor spheroids was quantified by assessing the proportion of red HUVECs within the green tumor area. Despite variability, overall penetration increased over time (Fig. 5D). On day 7, GBM spheroids demonstrated the highest level of penetration, significantly greater than that observed in Capan-2 spheroids (Fig. 5E). Higher penetration correlated with greater reductions in fused spheroid size, likely due to increased cell cohesion during fusion. The similar size reduction trends between tumor and fused spheroid sizes imply that increased cohesion within tumor spheroids drives fused spheroid contraction (Fig. S3). This behavior may encourage cytokine release and enhanced nutrient supply via penetrated vessels in a physiological environment, potentially accelerating tumor growth.

Images for morphology analysis were obtained from the 2D central section of the spheroids. Although HUVEC cells appeared to have penetrated, we needed to confirm whether the infiltration was due to penetration or the tumor encircling the HUVECs. Z-stack imaging with confocal microscopy at 20 μm intervals was conducted on the GBM-HUVEC fusion sample with the highest angiogenesis, allowing cell position analysis across layers (Fig. 5F). Throughout slices Z1 to Z6, tumor and HUVEC cells were evenly distributed, showing that the tumor did not enclose the HUVECs (Fig. 5H). Further, in regions where green tumor and red HUVEC cells were present, overlapping peaks in layers Z2 to Z4 and the diffused HUVEC's boundary indicated active HUVEC infiltration into the tumor (Fig. 5I). These findings reflect the tumor-driven angiogenesis process in a 3D context, where cytokines stimulate HUVEC sprouting and interaction with the tumor.

Based on our previous results, we performed qRT-PCR to further analyze the biological responses observed in the huvec/tumor fusion system (Fig. 5J). The mRNA expression level heatmap analysis showed that VEGF expression level was high in the GBM only group, but the expression level of VEGF-independent angiogenesis genes (*ANGPT1*, *CXCR2*) was relatively low in the Fusion group. On the other hand, compared to GBM only and GBM mixture groups, the Fusion group had

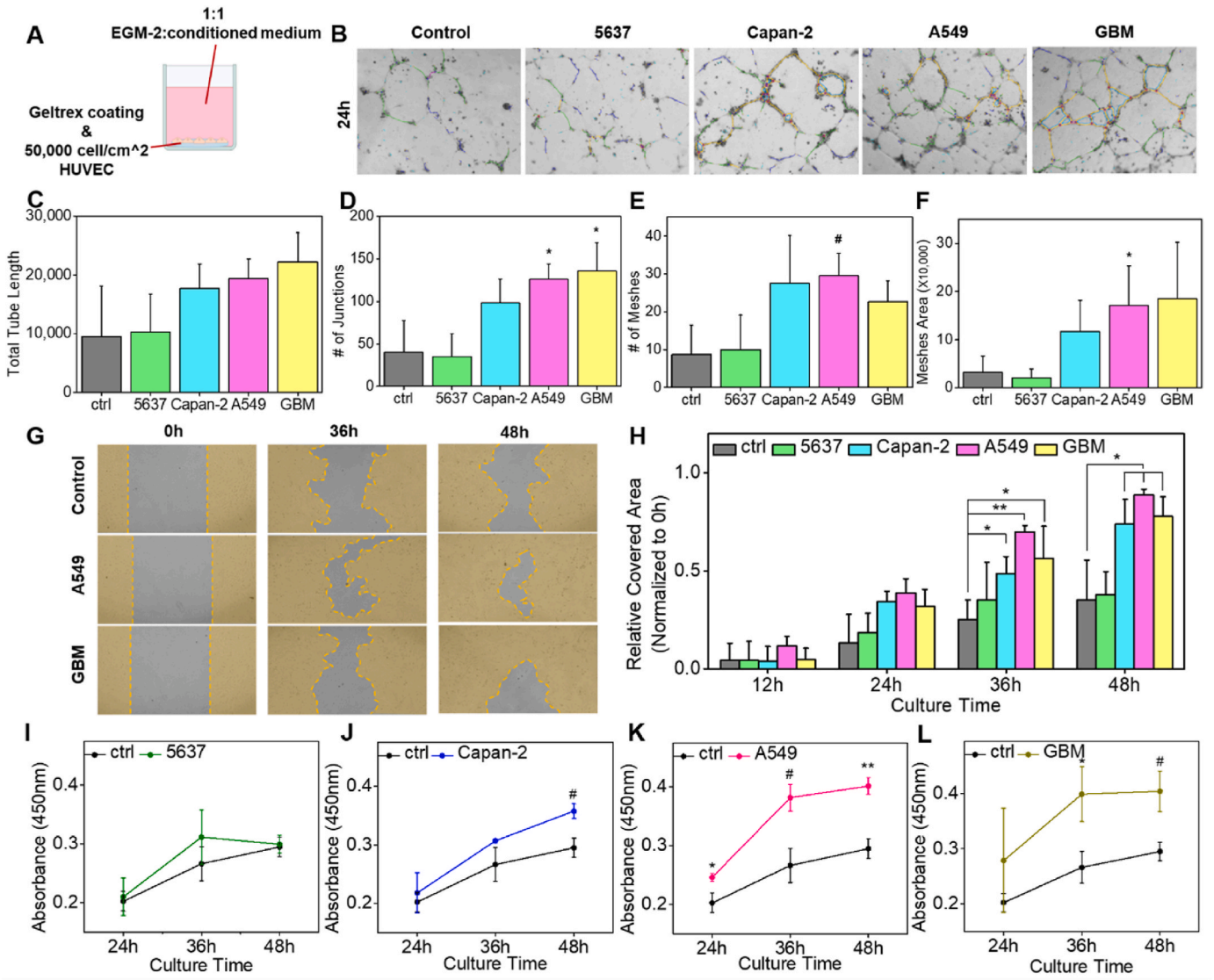

Fig. 3. Comparison of angiogenic ability of tumor CMs in 2D condition. (A) Schematic of the experimental setup. (B) Representative images of HUVEC tube formation in tumor CMs and control medium. (C–F) Quantification of total tube length, number of junctions, number of meshes, and mesh area (N = 4). (G) Representative images of wound healing assay after 0, 36 and 48h in tumor CMs and control medium. (yellow part: covered area) (H) Quantification of the HUVEC covered area after 12, 24, 36 and 48h. (normalized to initial uncovered area, N = 3) (I–L) Quantification of HUVEC proliferation in 5637, Capan-2, A549 and GBM CM compared to control medium after 24, 36 and 48h. (N = 3, **p < 0.005; #p < 0.01; *p < 0.05 based on ANOVA with Tukey HSD post hoc testing). (For interpretation of the references to color in this figure legend, the reader is referred to the Web version of this article.)

relatively higher expression levels of 1) VEGF-independent angiogenic genes (*ANGPT1*, *FLT1*, *KDR*, *PLGF*, *Col18a1*, *TIE1*), 2) endothelial cell-tumor cell interactions (*CD31*, *CDH5*, *Notch1*, *Notch2*, *THBS1*), and 3) cell migration and proliferation (*CD31*, *CDH5*, *Notch1*, *Notch2*, *THBS1*), 3) cell migration and proliferation (*FAK*, *AKT1*, *PLCG1*, *SRC*, *SOS1*, *TJP1*, *PAI1*), 4) signal transduction and regulation (*MAPK3*, *Stat3*, *MEK1*, *PIK3CD*), and 5) inflammation and immunomodulation (*CXCL16*, *CXCR2*, *TLR2*, *TLR4*, *TLR9*) were observed to be upregulated. These characteristics may indicate that the tumor microenvironment is more dynamic in the Fusion group compared to the other groups due to 1) increased endothelial cell-cell adhesion and vascular stability, 2) activation of cell migration and proliferation signals, and 3) upregulation of inflammatory and immune response regulation.

In order to explore in more detail, we assessed the expression of genes related to HUVEC proliferation and migration signaling, tight junctions, and tumor-driven angiogenesis (Fig. 5K). Compared to the simple mixture group, the fusion spheroid group showed a statistically significant increase in tumor derived angiogenesis related genes, tight junction genes, and signaling pathway genes. These results may indicate that the application of fusion of tumor cells and vascular cells not only affects the proliferation and angiogenesis of the blood vessels themselves, but also induces the formation of tight junctions between HUVECs and tumors, which may affect their stabilization. Furthermore, the activation of genes related to the MAPK/ERK pathway, which promotes cell proliferation and migration, further emphasizes the possibility of invasion or metastasis through the promotion of active cellular interactions between tumor cells and blood vessels.

The spheroid fusion system enabled a simulation of the angiogenesis process and facilitated tumor-HUVEC interactions, resulting in a more integrated and efficient vascularized tumor model. Comparisons across four cancer types within this system provided valuable insights. consistent with the 2D results, the fusion system showed increased sprouting and penetration in A549 and GBM, confirming that it effectively mimics angiogenesis. Additionally, the significant upregulation of angiogenesis-related genes in the fused system further supports its superiority over the simpler spheroid model.

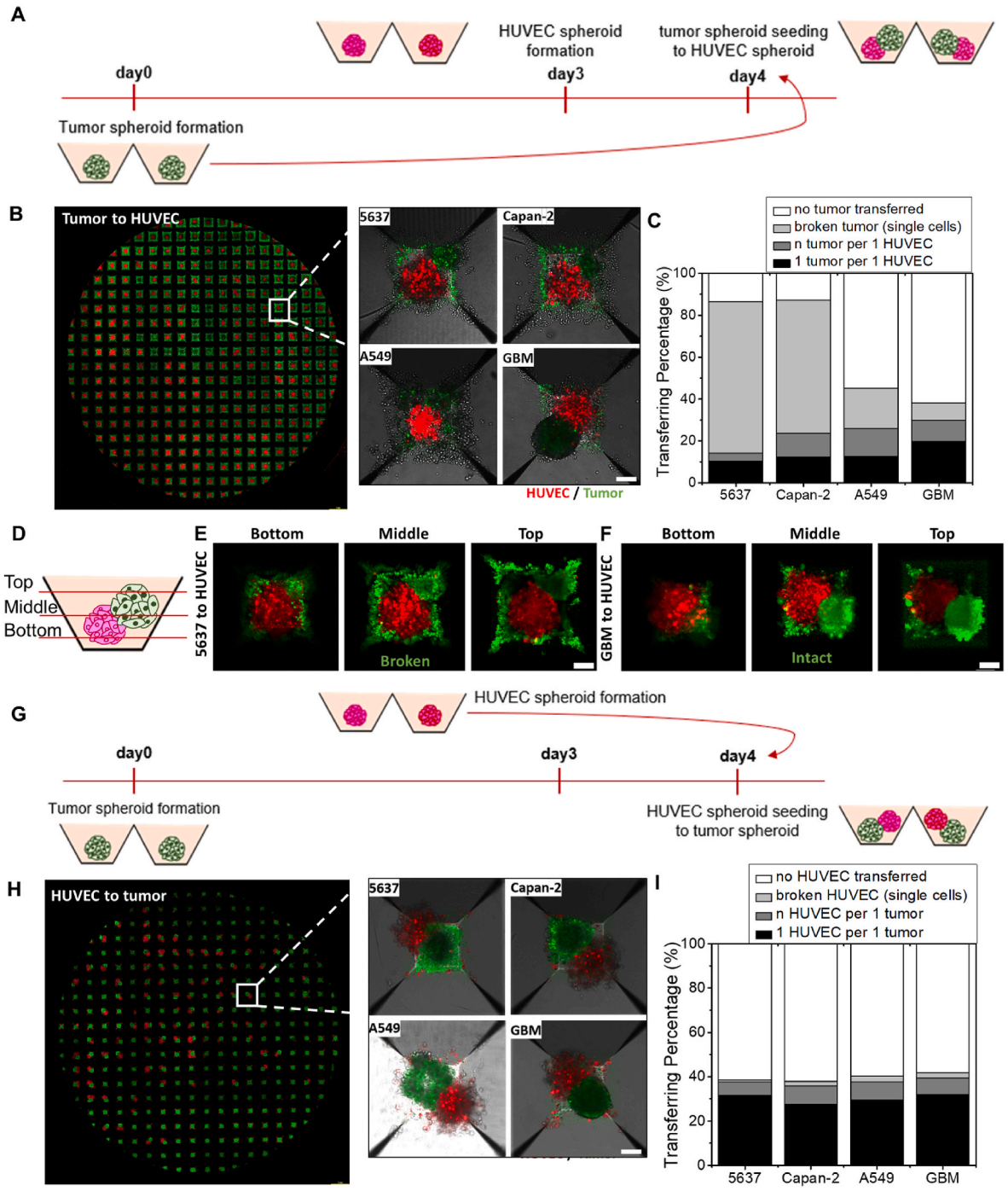

Fig. 4. Fabrication of tumor-HUVEC fusion spheroid system. (A) Illustration of timeline for tumor to HUVEC transfer system. (B) Confocal 3D images of the result of tumor to HUVEC transfer (HUVEC:red, tumor:geen). Large scale image is obtained from 5637 to HUVEC transfer. (C) Quantification of transferring percentages in tumor to HUVEC transfer system. (D) Illustration of transferred spheroid section. (E) Confocal image of broken transferred 5637 spheroid. (F) Confocal image of intact transferred GBM spheroid. (G) Illustration of timeline for HUVEC to tumor transfer system. (H) Confocal 3D images of the result of HUVEC to tumor transfer (HUVEC:red, tumor:geen). Large scale image is obtained from HUVEC to 5637 transfer. (I) Quantification of transferring percentages in HUVEC to tumor transfer system. Scale bars are all 100 μm. (For interpretation of the references to color in this figure legend, the reader is referred to the Web version of this article.)

2.5. *Angiogenesis related cytokines and genes analysis*

Following the observation of varying angiogenic abilities in four cancer types, we analyzed cytokines related to angiogenesis. One focus was VEGF, a primary factor in blood vessel growth [21]. Before comparing VEGF concentrations across various cancers, we validated the 3D spheroid system by assessing VEGF levels in cultures with an equal cell count in 2D and 3D conditions. VEGF secretion was greater in spheroid cultures than in 2D for both Capan-2 and GBM (least and most angiogenic in Fig. 4, respectively) (Fig. 6A). Longer spheroid culture durations increased VEGF secretion, widening the concentration difference between Capan-2 and GBM (Fig. 6B). To highlight these differences, we used 48-h culture CM to compare VEGF levels across tumors. The results, ranked as GBM, A549, 5637, and Capan-2 (Fig. 6C), mirrored previous angiogenesis trends, confirming VEGF's dominant influence.

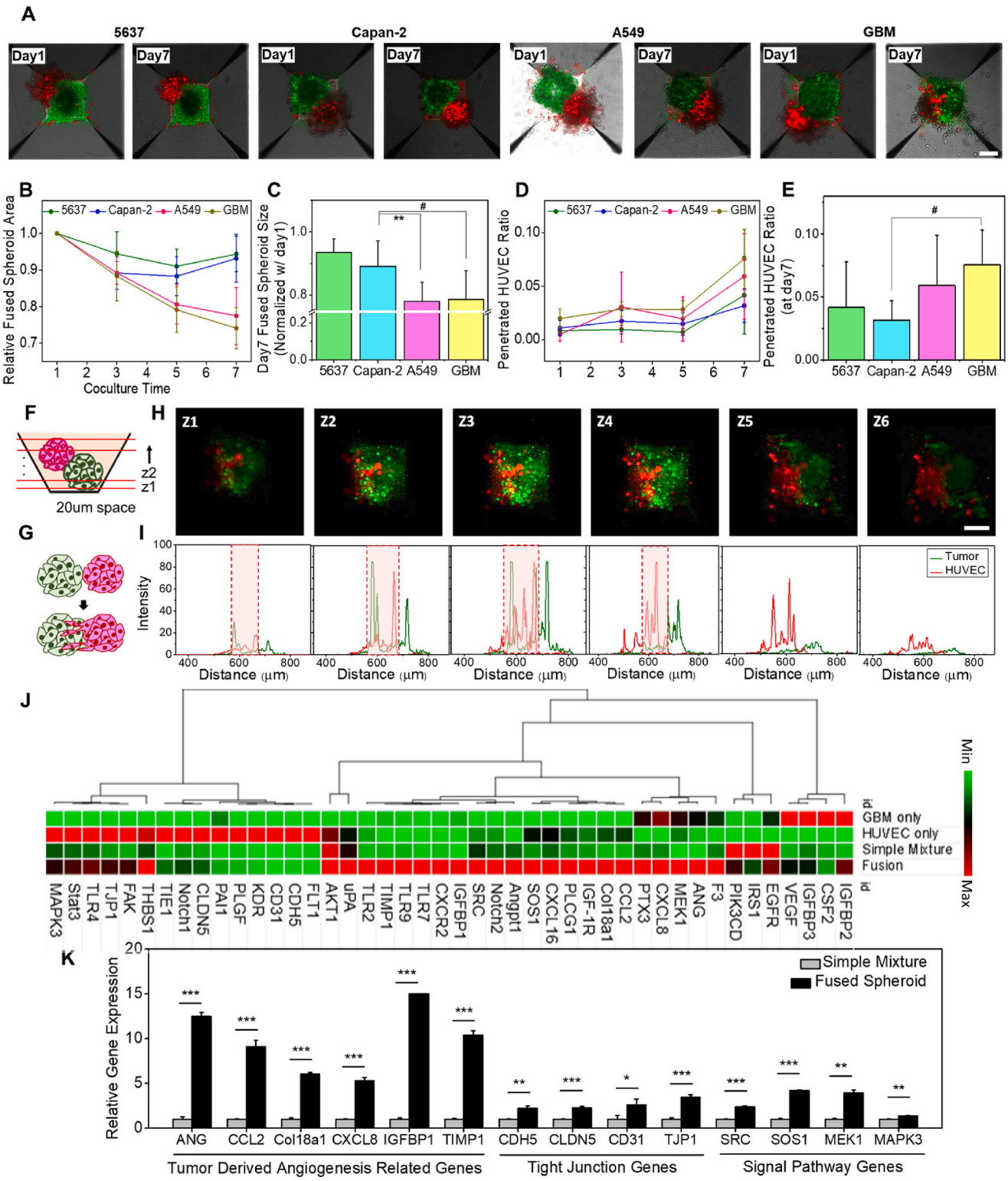

Fig. 5. 3D angiogenesis analysis in tumor-HUVEC fusion spheroid system. (A) Representative confocal 3D images of tumor-HUVEC fusion system at day1 and 7. (B) Quantification of fused spheroid area at day1, 3, 5 and 7. (data at day1 is normalized to 1) (C) Comparison of fused spheroid size at day7 ($N = 12$, $^{**}p < 0.005$; $\#p < 0.01$ based on ANOVA with Tukey HSD post hoc testing) (D) Quantification of penetrated HUVEC in tumor at day1, 3, 5 and 7. Area of HUVEC in tumor region is divided into area of tumor spheroid. (E) Comparison of penetrated HUVEC ratio at day7. (F) Illustration of fused spheroid section. ($N = 12$, $\#p < 0.01$ based on ANOVA with Tukey HSD post hoc testing) (G) Illustration of penetrating HUVEC into tumor. (H) Orthogonal views of confocal images of fused GBM-HUVEC spheroid. (HUVEC:red, GBM:green) (I) Plot profile of red HUVECs and green GBM cells. (Red box: penetrated area) (J) Heatmap of gene expression level through qRT-PCR. (K) Comparison of selective genes with significant difference between simple mixture of spheroids and fused spheroid. ($N = 3$, $^{***}p < 0.0005$; $^{**}p < 0.005$; $^{*}p < 0.05$ based on ANOVA with Tukey HSD post hoc testing) Scale bars are all 100 μm. (For interpretation of the references to color in this figure legend, the reader is referred to the Web version of this article.)

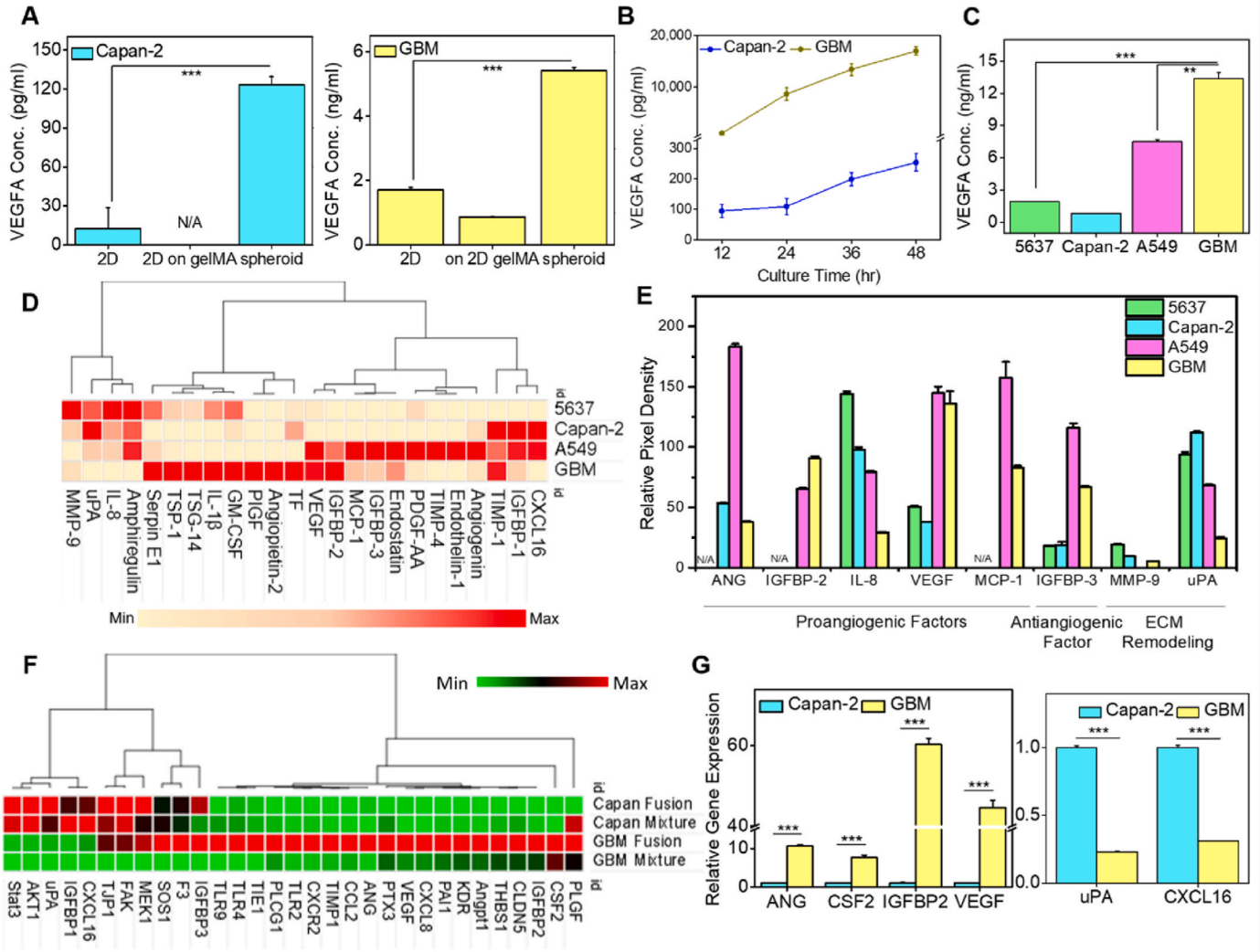

Fig. 6. Analysis of protein and gene expression about angiogenesis. (A) VEGF concentration of cancer cells (blue: Capan-2, yellow: GBM) in 2D culture and 3D spheroid culture. ($N = 3$, $^{***}p < 0.0005$ based on ANOVA with Tukey HSD post hoc testing) (B) VEGF concentration of tumor spheroids (blue: Capan-2, yellow: GBM) at 12h, 24h, 36h and 48h. (C) Comparison of VEGF concentration of tumors. ($N = 3$, $^{***}p < 0.0005$; $^{**}p < 0.005$ based on ANOVA with Tukey HSD post hoc testing) (D) Heatmap of relative expression levels of angiogenesis cytokine by tumor spheroids. (E) Comparison of selective cytokines with significant difference between high angiogenic tumors(A549, GBM) and low angiogenic tumors(5637, capan-2). (F) Heatmap of gene expression level through qRT-PCR. (G) Comparison of selective genes with significant difference between capan-2 fusion and GBM fusion. ($N = 3$, $^{***}p < 0.0005$ based on ANOVA with Tukey HSD post hoc testing). (For interpretation of the references to color in this figure legend, the reader is referred to the Web version of this article.)

Angiogenesis is not solely induced by VEGF; multiple cytokines are involved in this process [22]. To identify these additional cytokines, we conducted an angiogenesis cytokine array and identified 24 key cytokines displayed in a heat map (Fig. 6D). Most cytokines, except GM-CSF, IL-8, and uPA, were more abundant in the highly angiogenic A549 and GBM tumors. Among these, eight cytokines with marked differences between high and low angiogenic tumors were represented in a bar graph (Fig. 6E). ANG, IGFBP-2, VEGF, MCP-1, and IGFBP-3 were notably elevated in highly angiogenic cancers. Although IGFBP-3 is anti-angiogenic [23], its high levels in A549 and GBM may be counterbalanced by other pro-angiogenic factors. Additionally, MMP-9 and uPA, which support angiogenesis by remodeling ECM [24], were more prevalent in 5637 and Capan-2. However, their impact may be reduced in the absence of ECM in the in-vitro model.

To validate the results of the cytokine assay, gene expression levels were analyzed by qRT-PCR. Comparisons were made between fused spheroids from Capan-2 and GBM (least and most angiogenic in Fig. 4, respectively) and simple mixtures of cancer cells. A mRNA expression heatmap analysis results that the Capan-2 and GBM fusion models had different gene expression trends (Fig. 6F). In the GBM fusion model, we observed that gene expression related to 1) angiogenesis (*VEGF*, *Angpt1*, *FLT1*, *KDR*, *PLGF*, *Col18a1*, *TIE1*), 2) endothelial cell-tumor cell interaction (*CD31*, *CDH5*, *Notch1*, *Notch2*, *THBS1*), and 3) inflammation and immune regulation (*CXCR2*, *TLR2*, *TLR4*, *TLR9*, *CSF2*) were upregulated compared to the other groups. On the other hand, the Capan-2 fusion model is characterized by upregulation of genes related to 1) cell migration and proliferation (*FAK*, *AKT1*, *TJP1*) and 2) signal transduction and regulation (*MAPK3*, *Stat3*, *IRS1*, *MEK1*) compared to the GBM group. These findings suggest that when Capan-2 and GBM fuse with blood vessels, tumor characteristics differ, with GBM being a highly angiogenic tumor, while Capan-2 is more characterized by tumor cell migration and cell growth regulation. The distinct gene expression profiles observed in the GBM and Capan-2 fusion models reflect functional differences in their interactions with endothelial cells. In the GBM fusion system, upregulated genes related to VEGF-independent angiogenic signaling (e.g., ANGPT1, TIE1), endothelial stabilization (e.g., CDH5, Notch1/2), and inflammatory modulation (e.g., TLRs, CSF2) suggest the presence of a highly vascularized and immune-responsive

microenvironment. Conversely, the Capan-2 model predominantly upregulated genes involved in cell proliferation and migration (e.g., AKT1, MAPK3), indicating a more growth-driven but less angiogenic phenotype.

Genes showing patterns consistent with cytokine analysis results were normalized to Capan-2 fusion and visualized as bar graphs (Fig. 6G). The genes *ANG*, *CSF2*, *IGFBP2*, and *VEGF*, which are related to angiogenesis and vascular stability, were downregulated in GBM, while the genes *uPA* and *CXCL16*, which are related to cell migration and immune regulation, were upregulated in Capan-2. These results indicate that the fusion of tumor cells and vascular cells may affect the tumor microenvironment differently depending on the characteristics of the tumor cells, thereby affecting the proliferation, angiogenesis, and immunological response of the tumor. The role of uPA in ECM remodeling likely precluded its influence on angiogenesis [24b], while CXCL16, primarily involved in tumor proliferation [25], showed limited impact on angiogenesis within these fusion models.

In summary, cancer cells with enhanced angiogenic capability were found to express higher levels of angiogenesis-related genes and secrete a greater quantity of cytokines that promote angiogenesis. Not only was VEGF, a well-known angiogenic factor, secreted at high levels, but other significant angiogenic factors were also detected at elevated levels. These findings suggest that these factors collectively signal and interact, leading to the complex induction of angiogenesis.

2.6. Fluidic chip for drug test

A tumor-HUVEC fusion system was developed by encapsulating fused spheroids from Aggrewell in 7 % GelMA and loading them into PDMS fluidic chips. The details of the chip design are provided in Fig. 7A and Fig. S6. This setup mimics *in vivo* drug delivery by providing dynamic flow instead of static drug treatment while 7 % GelMA exhibits mechanical stiffness comparable to various tumor microenvironment to simulate physiological microenvironments (Fig. S7). The parallel connection of multiple fluidic devices enables simultaneous testing of multiple drugs or tumor types, facilitating high-throughput experiments (Fig. 7B). Beyond expanding experimental throughput, the platform allows the assessment of heterogeneous tumors under uniform conditions or screen multiple drugs on the same tumor model.

The GBM-HUVEC fused spheroid model, identified as highly vascularized, was validated for drug efficacy testing. Using the GBM-only and fused spheroid models, we investigated the uptake of doxorubicin

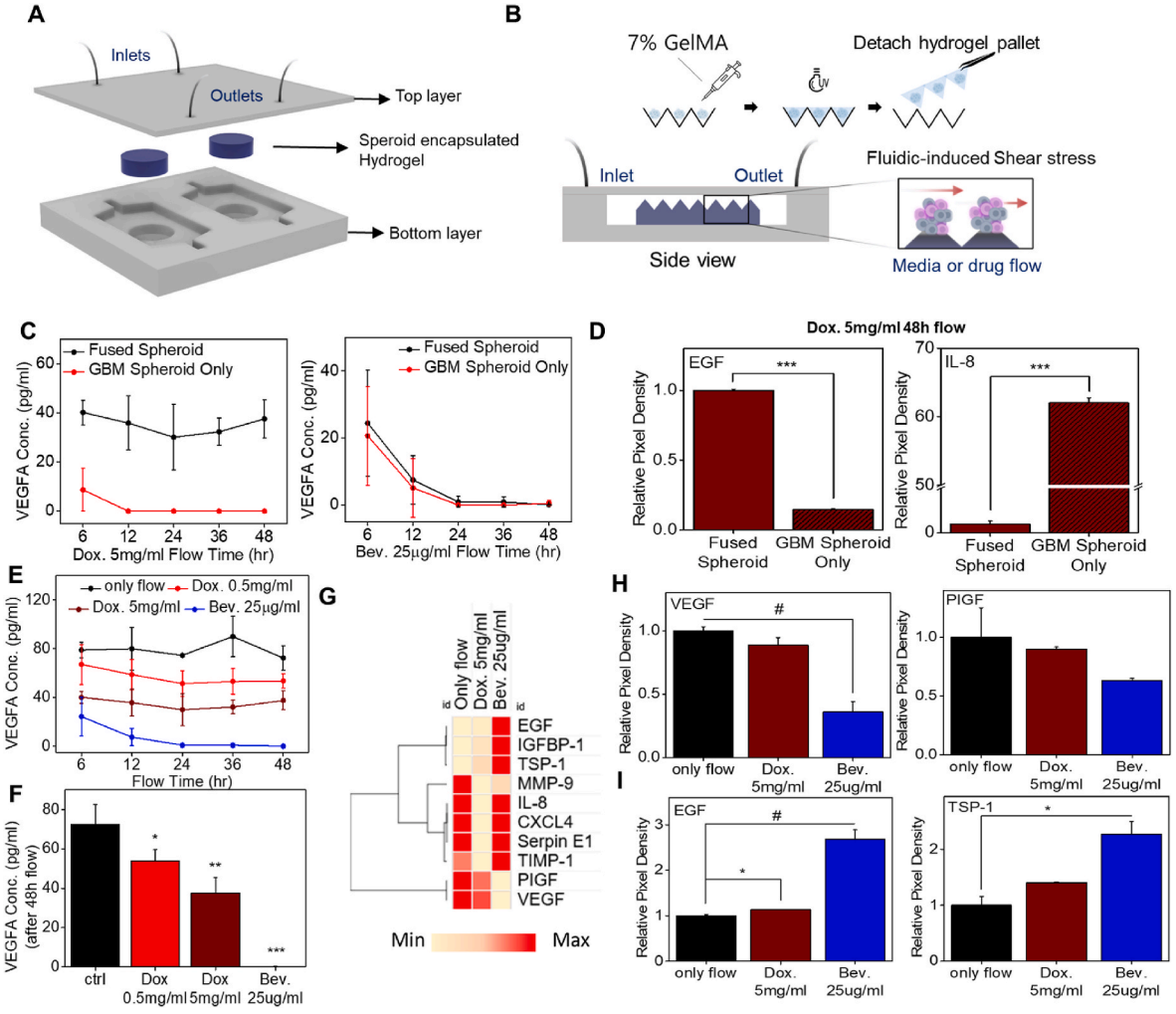

Fig. 7. Microfluidic chip for drug flow. (A) Design of the flow device. (B) Illustration of the fabrication and features of flow device. (C) Comparison of VEGF concentration after 48h of Doxorubicin and Bevacizumab flow on fused spheroid chip and GBM spheroid only chip. (D) Comparison of EGF and IL-8 after 48h of Dox flow between fused spheroid and GBM-only spheroid. ($N = 2$, $^{***}p < 0.0005$ based on ANOVA with Tukey HSD post hoc testing) (E) VEGF concentration after drug flow at 6h, 12h, 24h, 36h and 48h. (F) Comparison of VEGF concentration after 48h of drug flow. ($N = 3$, $^{**}p < 0.005$; $^{*}p < 0.05$ based on ANOVA with Tukey HSD post hoc testing) (G) Heatmap of relative expression levels of angiogenesis cytokines after drug flow. (H) Comparison of VEGF and PIGF after 48h of drugs flow. ($N = 2$, $\#p < 0.01$ based on ANOVA with Tukey HSD post hoc testing) (I) Comparison of EGF and TSP-1 after 48h of drugs flow. ($N = 2$, $\#p < 0.01$; $^{*}p < 0.05$ based on ANOVA with Tukey HSD post hoc testing).

(Dox.), a conventional chemotherapeutic, and bevacizumab (Bev.), a benchmark anti-angiogenic agent. VEGF secretion, measured by ELISA, was higher in fused spheroids than in GBM-only models for both Dox. and Bev. treatments (Fig. 7C). The slower drug action in fused spheroids was most prominent at high Dox doses, with VEGF secretion ceasing within 12 h in GBM-only but lasting up to 48 h in fused spheroids. Additionally, cytokine analysis following 48 h high-dose Dox. treatment confirmed the vascularized tumor model's effectiveness. In the GBM-only model, lower angiogenic EGF and higher pro-inflammatory IL-8 [26] levels indicated faster drug uptake (Fig. 7D). During the angiogenic process, a densely organized endothelial structure forms around the tumor spheroid, creating a functional vascular barrier that limits the diffusion of drugs and cytokines. This behavior closely reflects the barrier properties observed *in vivo*, reinforcing the fused spheroid model's relevance for evaluating therapeutic responses under more realistic conditions.

Further, to validate the platform's versatility, experiments were conducted using only flow conditions as controls, while Dox and Bev were tested under drug flow conditions to assess their effects on tumors. Experiments with doxorubicin were conducted at 0.5 mg/mL, the IC50 concentration for 2D cancer cells [27], and 5 mg/mL, a 10-fold higher dose. Bevacizumab was tested at 25 μg/mL, as suggested by drug test studies [28]. When drugs were flowed through fused spheroids, VEGF levels decreased with both Dox and Bev, correlating with increased flow time (Fig. 7E). After 48 h, VEGF levels significantly declined versus controls. Higher Dox concentrations further reduced VEGF secretion, and Bev nearly eliminated VEGF (Fig. 7F). Other angiogenic factors were also analyzed using a cytokine array of 48-h post-drug flow medium (Fig. 7G). Notably, VEGF and PIGF showed consistent pattern and EGF and TSP-1 showed similar pattern. VEGF levels decreased in Dox. flow and Bev. flow groups as seen in ELISA (Fig. 7H). PIGF secretion also decreased, which is expected given its VEGF subfamily relation [29] and Bev.'s VEGF-targeting effects [11b]. In contrast, EGF and TSP-1 showed significantly higher secretion in the Bev. flow group compared to only flow group (Fig. 7I). EGF, a factor promoting VEGF expression [30], likely upregulates to compensate for VEGF reduction from bevacizumab treatment. TSP-1, which can be induced by EGF [31], also exhibited a similar trend. These results highlight the ability of the tumor-HUVEC fusion spheroid system, when integrated into a fluidic device, to monitor drug responses via cytokine changes, enabling testing of various drugs under flow conditions.

2.7. *In vivo* study for verifying GBM-HUVEC fusion model

To confirm the angiogenic effect of the GBM-HUVEC fusion model *in vivo*, which was confirmed by the *in vitro* results, further analysis was performed using a mouse subcutaneous model. For this purpose, Gel only, HUVEC only (HUVEC spheroid), GBM only (GBM spheroid), and GBM + HUVEC spheroid (Fusion system) groups were implanted under the subcutaneous skin of nude mice and cultured for 1 and 3 weeks

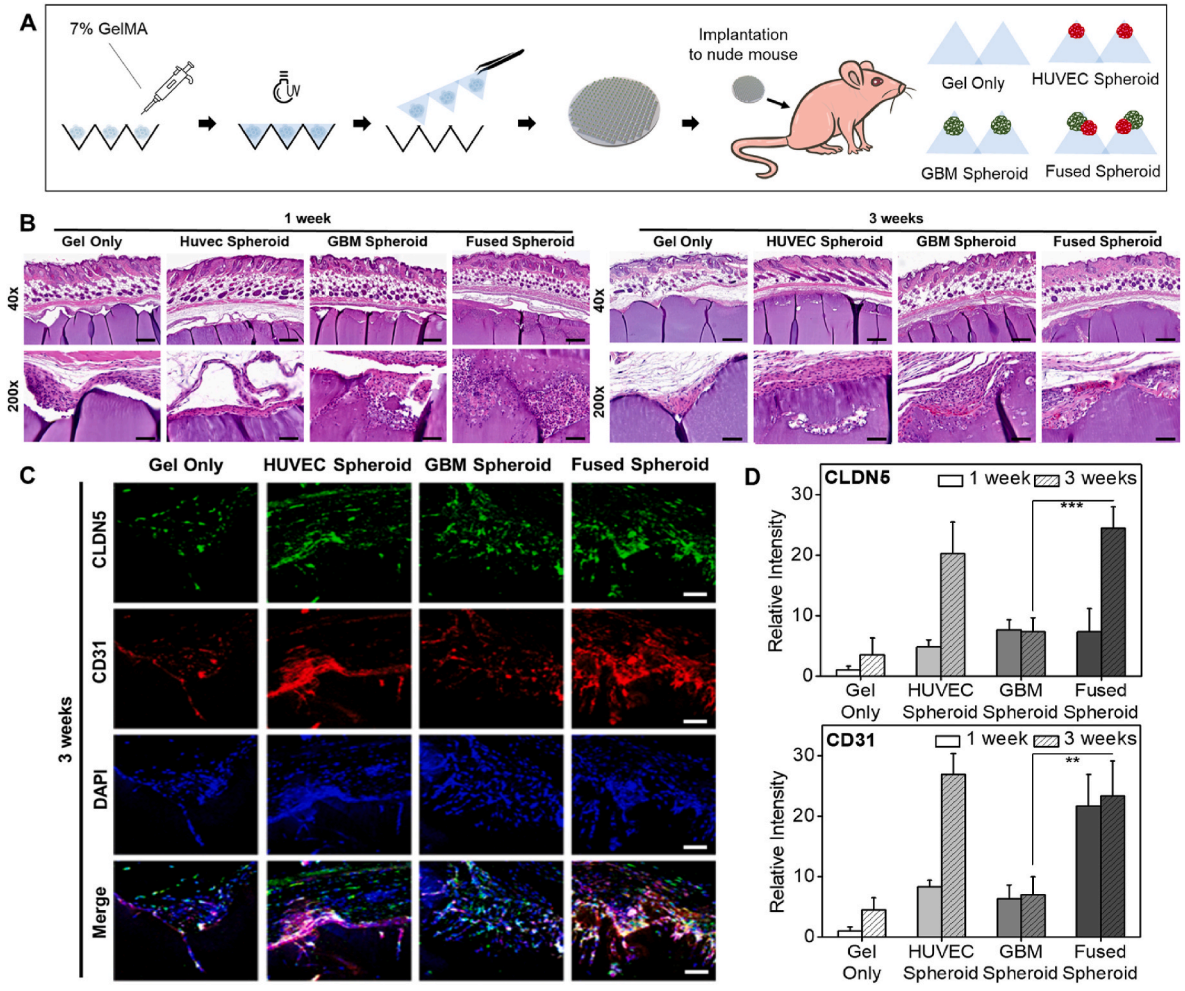

Fig. 8. Verification of results with *in vivo* study. (A) Illustration of the process of in-vivo study. (B) Images of H&E staining after 1 week and 3 weeks of implantation. Scale bars: 300 μm (40X), 60 μm (200X) (C) Images of immunofluorescence staining after 1 week and 3 weeks of implantation. Scale bars: 300 μm (D) Relative intensity of CLDN5 and CD31. ($N = 3$, $^{***}p < 0.0005$; $^{**}p < 0.005$ based on ANOVA with Tukey HSD post hoc testing).

(Fig. 8A). The toxicity analysis of vital organs (heart, lung, liver, kidney, spleen) following spheroid implantation showed that the implantation of each spheroid did not show significant toxicity except for mild to moderate splenic white pulp proliferation in the GBM and Fused spheroid groups (Fig. S8). Histopathologic analysis showed that the gel-only group had no significant expression of Cldn5 and CD31 other than a microscopic foreign body reaction at week 1, and no significant increase in expression at week 3. In the HUVEC spheroid group, a vascular-like structure was observed at week 1, which became more layered by week 3. At both week 1 and week 3, only the GBM and Fused spheroid groups showed foci of tumor proliferation (Fig. 8B).

Immunofluorescence staining results showed that the Gel only group showed low expression of vascular markers at week 1, while the HUVEC spheroid, GBM spheroid, and tumor-HUVEC fusion system groups showed higher expression of Cldn5 and CD31 compared to the Gel group. (Fig. S9). Interestingly, the expression of vascularization markers Cldn5 and CD31 was increased in the HUVEC and Fusion spheroid groups at week 3 (Fig. 8C). The marker of blood vessels and smooth muscle, α-SMA, was also found to be immuno-positive in the HUVEC and Fusion spheroid groups at higher levels than in the Gel only or GBM spheroid groups (Fig. S10). Quantitative analysis showed statistically significant elevated expression of Cldn5 and CD31 in the Fusion spheroid group at week 3 compared to the GBM spheroid group. These results are similar to our previous *in vitro* results, suggesting that the formation and stability of blood vessels is maintained in the fusion model of GBM tumor cells and HUVEC.

3. Conclusion

In this study, we established a tumor-HUVEC fusion spheroid system that enables robust vascularization through direct tumor–endothelial interactions, allowing for effective visualization of angiogenic processes in a 3D environment. By integrating tumor and endothelial cells, the model successfully replicates the complex tumor-vessel interactions observed in the tumor microenvironment. Additionally, we compared the angiogenic potential of various cancer types using the fusion spheroid system. Our findings demonstrate that tumor-derived factors significantly promote endothelial cell sprouting and migration. Furthermore, direct contact between tumor cells and HUVECs leads to the significant upregulation of angiogenesis-related genes, as validated both *in vitro* using fluidic chip platforms and *in vivo* in murine models. Although this system does not yet replicate long-term vascular maturation or immune–vascular crosstalk, this approach not only enhances the understanding of angiogenesis in cancer progression but also provides a promising *in vitro* platform for the testing and evaluation of anti-angiogenic drugs. The model has the potential to improve targeted therapeutic strategies and advance precision medicine in oncology.

4. Materials and methods

4.1. Cell lines and cell culture

The human bladder carcinoma cells (5637), human pancreas adenocarcinoma cells (Capan-2), human lung carcinoma cells (A549) and human glioblastoma cells (SNU-1105) were purchased from the Korean Cell Line Bank. The human primary umbilical vein endothelial cells (HUVEC) was purchased from the American Type Culture Collection (ATCC). The 5637, Capan-2, A549, GBM were cultured in Dulbecco's modified Eagle medium (DMEM, Gibco, USA) containing 10 % fetal bovine serum (FBS, Corning), 1 %(v/v) L glutamine (Gibco), and 100 μg/mL penicillin−streptomycin (Gibco, USA). The HUVEC was cultured in endothelial growth medium (EGM-2, Promocell) and was used at passage 6 through 9. All cells were maintained at 37 °C in a humidified atmosphere containing 5 % CO_2. The culture medium was changed every 3–4 days and the cells were passaged when 80–90 % confluence was reached.

4.2. Spheroid fabrication and characterization

Spheroids were formed using Aggrewell™ 800 plates (STEMcell Technologies) [16a]. Aggrewell plates were prepared by rinsing each well with 500 μL of Aggrewell Rinsing Solution (Stem Cell Technologies), spinning at 3000 RPM for 10 min to remove air bubbles in microwell and then washing wells with PBS. Tumor cells were seeded at a density of 9×10^5 cells/well to make spheroids of 3000 cells/spheroid in DMEM containing 1 % FBS and the HUVEC cells were seeded at a density of 4.5×10^5 cells/well to make spheroids of 1500 cells/spheroid in EGM-2 containing 10 % supplement. The culture medium was changed every 2 days.

After fabricating spheroids, morphology was imaged by optical microscopy (Nikon, TS100) - 2,3,5,7,9 days for tumor spheroids, 3,6,12,24 h for HUVEC. Diameter and circularity of spheroids were analyzed by ImageJ software.

Cell viability of spheroids was analyzed by a live/dead assay (Invitrogen, L3224) and it was used according to the manufacturer's instructions. The fluorescence image of core parts within the spheroids were obtained using a confocal microscope (Leica). The percentage of live/dead cells was measured by ImageJ software from 9 randomly selected microwells of aggrewell for each group.

4.3. Preparation of CM for angiogenic ability tests

To assess the effect of tumor on angiogenic ability of HUVEC, conditioned medium (CM) of each tumor spheroids was used. The CM of spheroids was collected the day after their formation. To supplement nutrients needed for the cell culture assays, each CMs of spheroids were mixed with fresh basal EGM-2 (EGM-2 without supplementMix) containing 10 % FBS in a 1:1 ratio; this mixture is termed the tumor-CM. A negative control was a 1:1 mixture of fresh DMEM containing 1 % FBS (non-conditioned spheroid medium) and basal EGM-2 containing 10 % FBS.

4.4. Tube formation assay

Tube formation assay was performed on a 24-well plate coated with Geltrex™ (Gibco) [19a]. 150 μl of geltrex™ was loaded per each well of 24-well plate and incubated at 37 °C for 30 min for gelation. HUVECs were seeded at a density of 9×10^4 cells/well in 0.5 ml tumor-CM or control medium. After 24h, the phase contrast images of each wells were obtained by fluorescence microscopy (Nikon, Ti2). Various descriptors of capillary-like tube formation (total tube length, number of junctions, number of meshes, meshes area) were analyzed using the 'Angiogenesis Analyzer' plugin for ImageJ software [32]. The assay of each tumor was performed in triplicate.

4.5. Wound healing assay

The cell migration was assessed by wound healing assay on a 48-well plate coated with gelatin. 2 % gelatin was sterilized and coated on each well. To keep the intact gelatin coating, physical barrier assay was selected to assess cell migration [33]. 200 μm width of PMMA fence was cut by laser cutter (Rexbot) and placed into each well. HUVECs were seeded at a density of 2×10^4 cells/well in EGM-2. After incubation overnight, the fence was removed and medium was changed into tumor-CM or control medium. The wound sites were imaged using optical microscopy after 0h, 6h, 24h, 36h and 48h and the covered area was analyzed by imageJ software. The assay of each tumor was performed in triplicate.

4.6. WST-8 assay

Proliferation of HUVEC was assessed using the quantitative colorimetric WST-8 assay (BIOMAX) at 3 time-points (24h, 36h, 48h). It was

performed by manufacturer's instructions. Briefly, HUVEC cells were seeded at a density of 2x103 cells/well in 200 μl EGM-2 in 96-well plate. After incubation overnight, the medium was changed into 100 μl of tumor-CM or control medium. After 24h, 36h or 48h, 10 μl of WST-8 solution was added to each well and incubated for 2h. The absorbance was measured by microplate reader (Tecan) at a wavelength of 450 nm with a reference wavelength of 600 nm. Each assay was performed in triplicate.

4.7. Cell tracking in spheroids

To observe the location of tumor cells and HUVECs, each cell was labeled with cell trackers before making spheroids. CMFDA (Invitrogen, CellTracker Green C2925) and CM-DiI (Invitrogen, CellTracker CM-DiI C7001) were used for tumor cells and HUVEC respectively. Stock solutions of each cell trackers were prepared in 10 mM concentration and then working solution were made by 1000x diluting stock solutions in phosphate buffered saline (PBS, T&I). Cells in CMFDA working solution were incubated at 37 °C for 30 min and cells in CM-DiI working solution were incubated at 37 °C for 5 min and 4 °C for 15 min. After incubation, cells were centrifuged, resuspended in fresh medium and seeded in aggrewell to form fluorescence labeled spheroids. 3000 cells/spheroid of tumor spheroids and 1500 cells/spheroid of HUVEC spheroids were fabricated as mentioned above. After spheroid formation, the samples were incubated wrapping by foil to shield from light.

4.8. Fused spheroid fabrication and characterization

To form fused spheroids, tumor spheroids were incubated for 4 days and HUVEC spheroids were incubated for 1 day, respectively. Tumor spheroids (HUVEC spheroids) were transferred into the well containing HUVEC spheroids (tumor spheroids) by very gently pipetting. After overnight incubation to sink the transferred spheroids, the medium was changed into fresh mixed spheroid medium. The mixed medium is the mixture of 67 % (v/v) DMEM containing 1 % FBS and 33 % (v/v) EGM-2 containing 10 % supplement which is a volume ratio set proportionally to the number of cells in each well.

The morphology of fused spheroids was imaged in fluorescence images using confocal microscopy. 10 Microwells with 1 tumor spheroid and 1 HUVEC spheroid were randomly selected and imaged continuously every 2 days for characterization. The characterization of fused spheroids (size of fused spheroids and penetrated area) was performed using ImageJ software.

4.9. VEGFA ELISA

The concentration of VEGFA in the conditioned medium were quantified using VEGFA ELISA (ABClonal, RK00023) following the manufacturer's instructions. OD values were averaged from duplicates, background-corrected using the zero standard, and analyzed using a four-parameter logistic (4-PL) standard curve. Final concentrations were adjusted for any dilution factors. All samples were collected under standardized conditions with equal cell numbers across groups, as determined by prior spheroid optimization (Fig. 2). VEGF concentrations were reported as absolute values (pg/mL) without additional normalization to cell number. For the experiment, cell culture mediums of each tumor spheroids were collected at 4 time points (12h, 24h, 36h, 48h) in advance.

To compare 2D and 3D condition additionally, the same number of cells as the number in 1 well of spheroids was seeded on 2D culture well plate and on gelMA coated wellplate. The conditioned culture medium was collected from each well after 24h and it was used in ELISA experiments in the same way as mentioned above.

4.10. Human angiogenesis array

The cytokines associated with angiogenesis were assessed utilizing the Proteome profiler human angiogenesis array kit (R&D Systems, ARY007) by the manufacturer's instruction, chemiluminescence was detected and analyzed by CCD imager (Cytiva, Amersham™ ImageQuant™ 800). For the experiment, cell culture mediums of each tumor spheroids were collected at 48h and stored immediately at −80 °C.

4.11. qRT-PCR

For qRT-PCR analysis, spheroids were collected by floating them in Aggrewell and subsequently pelleting them in conical tubes. After resuspension in PBS and washing via centrifugation, the supernatant was carefully removed, and the cells were preserved at −80 °C until analysis. Total RNA was extracted following the manufacturer's protocol using the NucleoSpin RNA Plus kit (Macherey-Nagel, USA). The extracted RNA was then used to synthesize cDNA with the ReverTra Ace qPCR RT Kit (Toyobo, Japan). Real-time PCR was performed for 45 cycles using the Thunderbird Next SYBR qPCR Mix (Toyobo). The primers that were used for qRT-PCR are listed in Table S1 of the Supporting Information. The expression levels were normalized using the average values of glyceraldehyde 3-phosphate dehydrogenase (GAPDH), beta-actin (β-actin), and 18s ribosomal RNA (18s rRNA) as reference genes. GBM only(for Fig. 5) or Capan Fusion (for Fig. 6) served as the control group, and gene expression levels were quantified using the $2^{-\Delta\Delta CT}$ method, representing fold changes in threshold cycle (Ct) values.

4.12. Microfluidic chip fabrication

The PDMS microfluidic chip was fabricated by pouring a 10:1 PDMS prepolymer mixture into a PMMA mold, which was laser-cut and bonded. The mixture was degassed and cured at 80 °C for 1 h. After demolding, inlet and outlet holes of 1.5 mm diameter were punched. The dimensions of the chip are expressed in Fig. S6.

After gently removing the media from the aggrewell containing fused spheroids, 500 μL of 7 % GelMA (with 0.5 % Irgacure 2959) was added [34]. The GelMA was crosslinked under UV light for 2 min, detached from the aggrewell, and loaded into a PDMS chip. Prior to GelMA loading, the PDMS chip was treated with O_2 plasma and immediately bonded upon GelMA addition. Finally, a medium containing either control or drugs (Doxorubicin 0.5 mg/mL, 2.5 mg/mL; Bevacizumab 25 μg/mL) was perfused at 10 μL/min. A previous study from our group performed a computational fluid dynamics (CFD) simulation using the same device design to validate flow behavior, including shear stress distribution and velocity profiles [35].

4.13. In vivo study

Using Aggrewell, spheroids were formed, cultured for 4 days and encapsulated in 7 % GelMA. Cell-loaded constructs were subcutaneously implanted in nude mice (male, 7 weeks). Twenty-four nude mice (OrientBio, Korea) were divided into four groups: Gel, Huvec, GBM, and fusion groups. All animal experiments were conducted in accordance with the guidelines of the Korea University Institutional Animal Care and Use Committee (approval number: KUIACUC-2024-0078). Antibiotics (enrofloxacin) and analgesics (carprofen) were administered before and immediately after surgery to prevent pain and infection. Under the anesthesia chamber, inhalational anesthesia was induced using 4 % isoflurane and then maintained with 1.5–2.5 % isoflurane. The dorsal skin was disinfected twice with povidone/70 % alcohol, and then blunt scissors were used to create a subcutaneous pocket by making an approximately 1 cm incision using Metzenbaum scissors. Circular samples with a diameter of 6 mm were implanted in the subcutaneous pocket. The incisions were closed using 4-0 non-absorbable suture

material and surgical clips. Three animals per group were sacrificed at weeks 1 and 3 of post-implantation, and the implanted skin/cell-loaded structures and vital organs (heart, lung, liver, kidney, spleen) were harvested. The harvested tissues were fixed and stored in 4 % neutralized buffered formalin (NBF) for histopathological evaluation.

4.14. Histopathological evaluation

For histopathologic analysis, formalin-fixed samples were trimmed and then dehydrated/paraffin-embedded using conventional paraffin tissue processing methods. Using a microtome, paraffin block samples were cut into 4–5 μm thick sections, deparaffinized/rehydrated, and stained with hematoxylin and eosin (HE). The stained slides were embedded with mounting medium and imaged using an inverted light microscope (Amscope, USA).

For immunofluorescence staining, the sectioned slides were deparaffinized/rehydrated and subjected to pressurized antigen retrieval (Abcam, USA) in citrate buffer. Normal goat serum was used as blocking solution for 30 min. Then, primary antibodies were incubated for 2 h. The primary antibodies used are as follows: anti-CD31 antibody (Santa Cruz, 1:100, USA), anti-Cldn5 antibody (ABclonal, 1:100, USA), and anti-α-sma antibody (Santa Cruz, 1:100). The secondary antibodies were anti-mouse IgG Texas Red-X (ThermoFisher, 1:200, USA), anti-rabbit IgG Alexa Fluor 488 (ThermoFisher, 1:200). The secondary antibodies were incubated for 1 h at room temperature. Subsequently, counterstaining and embedding were performed using Vectashield Hardset Antifade Mounting Medium with DAPI. Immunofluorescence-stained slides were photographed using a Zeiss confocal microscope (Zeiss AxioObserver Z1 microscope), and the intensity of fluorescence was analyzed using Zen Blue (Zeiss) software and Image J software.

4.15. Statistical analysis

For morphology analysis, raw images were analyzed. Results were derived from three replicates. Data presentation included mean ± standard deviation. Statistical significance was assessed using One-way ANOVA with Tukey HSD (Honestly Significant Difference) post-hoc test (http://statpages.info/anova1sm.html). (*$p < 0.05$, $^{\#}p < 0.01$, **$p < 0.005$, ***$p < 0.0005$)

CRediT authorship contribution statement

Suyeon Shin: Writing – original draft, Visualization, Validation, Methodology, Investigation, Formal analysis, Data curation, Conceptualization. **Yurim Choi:** Writing – original draft, Visualization, Validation, Methodology, Investigation, Formal analysis, Data curation, Conceptualization. **WonJun Jang:** Visualization, Validation, Investigation, Formal analysis. **Batjargal Ulziituya:** Writing – original draft, Visualization, Formal analysis. **Giheon Ha:** Visualization, Validation, Investigation, Formal analysis. **Raehui Kang:** Visualization, Validation, Investigation, Formal analysis. **Soojin Park:** Visualization, Validation, Investigation, Formal analysis. **Minseok Kim:** Visualization, Validation, Investigation, Formal analysis. **Yu Shrike Zhang:** Writing – review & editing, Validation. **Han-Jun Kim:** Writing – original draft, Visualization, Validation, Supervision, Project administration, Methodology, Formal analysis, Conceptualization. **Junmin Lee:** Writing – original draft, Visualization, Validation, Supervision, Funding acquisition, Conceptualization.

Data and materials availability

All data required to assess the conclusions of this study are included in the paper and/or the Supplementary Materials. Further data related to this paper are available from the corresponding author upon reasonable request.

Declaration of competing interest

The authors declare that they have no known competing financial interests or personal relationships that could have appeared to influence the work reported in this paper.

Acknowledgments

The authors gratefully acknowledge funding from National Research Foundation of Korea (NRF) grant (RS-2023-00211096, RS-2023-00260454, and RS-2024-00403376) funded by the Korean government (MSIT) as well as Glocal University 30 Projects (Biomedical Engineering Center). This work was partly supported by the Institute of Information & Communications Technology Planning & Evaluation(IITP)-ITRC(Information Technology Research Center) grant funded by the Korea government(MSIT) (IITP-2025-RS-2023-00258971). Authors also thank Prof. Seung Soo Oh at POSTECH MSE for help with confocal imaging.

Appendix A. Supplementary data

Supplementary data to this article can be found online at https://doi.org/10.1016/j.mtbio.2025.101741.

Data availability

Data will be made available on request.

References

[1] R.L. Siegel, K.D. Miller, N.S. Wagle, A. Jemal, Ca - Cancer J. Clin. 73 (2023) 17.
[2] a) F.R. Balkwill, M. Capasso, T. Hagemann, J. Cell Sci. 125 (2012) 5591;
b) A.S. Nunes, A.S. Barros, E.C. Costa, A.F. Moreira, I.J. Correia, Biotechnol. Bioeng. 116 (2019) 206.
[3] a) L. Nagl, L. Horvath, A. Pircher, D. Wolf, Front. Cell Dev. Biol. 8 (2020) 766;
b) D. Klein, Front. Oncol. 8 (2018) 367.
[4] a) Z.-L. Liu, H.-H. Chen, L.-L. Zheng, L.-P. Sun, L. Shi, Signal Transduct. Targeted Ther. 8 (2023) 198;
b) A. Fadaka, B. Ajiboye, O. Ojo, O. Adewale, I. Olayide, R. Emuowhochere, Journal of Oncological Sciences 3 (2017) 45.
[5] R. Edmondson, J.J. Broglie, A.F. Adcock, L. Yang, Assay and Drug Development Technologies, vol. 12, 2014, p. 207.
[6] a) B.M. Baker, C.S. Chen, J. Cell Sci. 125 (2012) 3015;
b) E.C. Costa, A.F. Moreira, D. de Melo-Diogo, V.M. Gaspar, M.P. Carvalho, I. J. Correia, Biotechnol. Adv. 34 (2016) 1427.
[7] M. Dey, B. Ayan, M. Yurieva, D. Unutmaz, I.T. Ozbolat, Advanced biology 5 (2021) 2100090.
[8] a) S. Chuaychob, R. Lyu, M. Tanaka, A. Haginiwa, A. Kitada, T. Nakamura, R. Yokokawa, Proceedings of, vol. 121, the National Academy of Sciences, 2024 e2312472121;
b) H. Kim, B. Kim, S.J. Kim, Y. Choi, I.H.R. Kim, J. Han, Y.G. Park, Y.M. Han, J. K. Park, Adv. Healthcare Mater. (2024) 2400501;
c) J. Ko, J. Ahn, S. Kim, Y. Lee, J. Lee, D. Park, N.L. Jeon, Lab Chip 19 (2019) 2822.
[9] S.M. Weis, D.A. Cheresh, Nat. Med. 17 (2011) 1359.
[10] M.R. Junttila, F.J. De Sauvage, Nature 501 (2013) 346.
[11] a) S. Guelfi, K. Hodivala-Dilke, G. Bergers, Nat. Rev. Cancer 1 (2024);
b) H. Hurwitz, L. Fehrenbacher, W. Novotny, T. Cartwright, J. Hainsworth, W. Heim, J. Berlin, A. Baron, S. Griffing, E. Holmgren, N. Engl. J. Med. 350 (2004) 2335;
c) L. Zhong, Y. Li, L. Xiong, W. Wang, M. Wu, T. Yuan, W. Yang, C. Tian, Z. Miao, T. Wang, Signal Transduct. Targeted Ther. 6 (2021) 1.
[12] a) Y. Zhou, X. Chen, J. Cao, H. Gao, J. Mater. Chem. B 8 (2020) 6765;
b) M.W. Dewhirst, T.W. Secomb, Nat. Rev. Cancer 17 (2017) 738;
c) J. Rodrigues, M.A. Heinrich, L.M. Teixeira, J. Prakash, Trends in cancer 7 (2021) 249.
[13] J. Park, S. Kim, J. Hong, J.S. Jeon, Lab Chip 22 (2022) 4335.
[14] a) K. Haase, G.S. Offeddu, M.R. Gillrie, R.D. Kamm, Adv. Funct. Mater. 30 (2020) 2002444;
b) D.T. Phan, X. Wang, B.M. Craver, A. Sobrino, D. Zhao, J.C. Chen, L.Y. Lee, S. C. George, A.P. Lee, C.C. Hughes, Lab Chip 17 (2017) 511;
c) C.W. McAleer, C.J. Long, D. Elbrecht, T. Sasserath, L.R. Bridges, J.W. Rumsey, C. Martin, M. Schnepper, Y. Wang, F. Schuler, Sci. Transl. Med. 11 (2019) eaav1386.
[15] a) J. Friedrich, C. Seidel, R. Ebner, L.A. Kunz-Schughart, Nat. Protoc. 4 (2009) 309;
b) Y. Markovitz-Bishitz, Y. Tauber, E. Afrimzon, N. Zurgil, M. Sobolev, Y. Shafran,

A. Deutsch, S. Howitz, M. Deutsch, Biomaterials 31 (2010) 8436;
c) R.M. Sutherland, J.A. McCredie, W.R. Inch, J. Natl. Cancer Inst. 46 (1971) 113.
[16] a) G. Razian, Y. Yu, M. Ungrin, J. Vis. Exp. 81 (2013) e50665;
b) K. Wrzesinski, A. Rogowska-Wrzesinska, R. Kanlaya, K. Borkowski, V. Schwämmle, J. Dai, K.E. Joensen, K. Wojdyla, V.B. Carvalho, S.J. Fey, PLoS One 9 (2014) e106973.
[17] M. Astolfi, B. Péant, M. Lateef, N. Rousset, J. Kendall-Dupont, E. Carmona, F. Monet, F. Saad, D. Provencher, A.-M. Mes-Masson, Lab Chip 16 (2016) 312.
[18] R. Auerbach, R. Lewis, B. Shinners, L. Kubai, N. Akhtar, Clin. Chem. 49 (2003) 32.
[19] a) I. Arnaoutova, H.K. Kleinman, Nat. Protoc. 5 (2010) 628;
b) K.L. DeCicco-Skinner, G.H. Henry, C. Cataisson, T. Tabib, J.C. Gwilliam, N. J. Watson, E.M. Bullwinkle, L. Falkenburg, R.C. O'Neill, A. Morin, J. Vis. Exp. (2014) 51312.
[20] a) M. Palmiero, I. Cantarosso, L. di Blasio, V. Monica, B. Peracino, L. Primo, A. Puliafito, Mol. Oncol. 17 (2023) 1699;
b) J. Kim, J. Jang, D.-W. Cho, Front. Bioeng. Biotechnol. 9 (2021) 605819;
c) Z.N. Abbas, A.Z. Al-Saffar, S.M. Jasim, G.M. Sulaiman, Sci. Rep. 13 (2023) 18380.
[21] L. Claesson-Welsh, M. Welsh, J. Intern. Med. 273 (2013) 114.
[22] a) N. Nishida, H. Yano, T. Nishida, T. Kamura, M. Kojiro, Vascular Health and Risk Management, vol. 2, 2006, p. 213;
b) A. Karamysheva, Biochemistry (Mosc.) 73 (2008) 751.
[23] H.-J. Shih, H.-F. Chang, C.-L. Chen, P.-L. Torng, Sci. Rep. 11 (2021) 22925.
[24] a) K.E. Rodrigues, M.H.B. Pontes, M.B.S. Cantão, A.F. Prado, Pharmacol. Res. (2024) 107285;
b) A. Micalet, L.J. Tappouni, K. Peszko, D. Karagianni, A. Lam, J.R. Counsell, S. A. Quezada, E. Moeendarbary, U. Cheema, Matrix Biol. 19 (2023) 100137.
[25] L. Deng, N. Chen, Y. Li, H. Zheng, Q. Lei, Biochim. Biophys. Acta Rev. Canc 1806 (2010) 42.
[26] M.C. Cesta, M. Zippoli, C. Marsiglia, E.M. Gavioli, F. Mantelli, M. Allegretti, R. A. Balk, Front. Pharmacol. 12 (2022) 808797.
[27] M. Norouzi, V. Yathindranath, J.A. Thliveris, B.M. Kopec, T.J. Siahaan, D. W. Miller, Sci. Rep. 10 (2020) 11292.
[28] a) S. Tabasum, D. Thapa, A. Giobbie-Hurder, J.L. Weirather, M. Campisi, P. J. Schol, X. Li, J. Li, C.H. Yoon, M.P. Manos, Cancer Immunol. Res. 11 (2023) 1493;
b) D. Klaver, H. Gander, G. Dobler, A. Rahm, M. Thurnher, Cell. Mol. Life Sci. 79 (2022) 519.
[29] S. De Falco, Exp. Mol. Med. 44 (2012) 1.
[30] a) G. Niu, K.L. Wright, M. Huang, L. Song, E. Haura, J. Turkson, S. Zhang, T. Wang, D. Sinibaldi, D. Coppola, Oncogene 21 (2002) 2000;
b) J. Tabernero, Mol. Cancer Res. 5 (2007) 203.
[31] M. Soula-Rothhut, C. Coissard, H. Sartelet, C. Boudot, G. Bellon, L. Martiny, B. Rothhut, Exp. Cell Res. 304 (2005) 187.
[32] G. Carpentier, S. Berndt, S. Ferratge, W. Rasband, M. Cuendet, G. Uzan, P. Albanese, Sci. Rep. 10 (2020) 11568.
[33] R. Riahi, Y. Yang, D.D. Zhang, P.K. Wong, J. Lab. Autom. 17 (2012) 59.
[34] J.W. Nichol, S.T. Koshy, H. Bae, C.M. Hwang, S. Yamanlar, A. Khademhosseini, Biomaterials 31 (2010) 5536.
[35] J. Song, Y. Lee, M. Kim, G. Ha, W. Jang, U. Batjargal, Y.G. Kim, H. Kim, J. Lee, Lab Chip (2025), https://doi.org/10.1039/D4LC00950A.